Application of the Hybrid Finite-Difference Time-Domain Method to Modeling Curved Surfaces in Three-Dimensional Lithography Simulation

Michael S. Yeung and Eytan Barouch
Department of Manufacturing Engineering, Boston University, Boston, MA 02215

ABSTRACT

The original hybrid-FDTD method developed by Wu and Itoh is extended to handle lossy materials with positive or negative dielectric constants. Numerical results are given to compare the hybrid-FDTD method and standard FDTD. The results show that the hybrid-FDTD method is much more accurate than standard FDTD when the same mesh spacing is used in both methods. In the case of lossy materials with negative dielectric constants, the hybrid-FDTD method is found to be much more accurate than standard FDTD even when a mesh spacing four times finer is used in the latter method. These results highlight the importance of modeling curved surfaces accurately in DUV lithography simulation using the hybrid-FDTD method.

Keywords: p hotolithography simulation, hybrid finite difference time domain method

1. INTRODUCTION

Electromagnetic scattering from nonplanar topography on the mask or wafer can have a significant impact on photomask performance, linewidth control or alignment precision. Computer simulation is a cost-effective way to assess the importance of such electromagnetic scattering effects in photolithography. With the scaling of devices to smaller dimensions, greater demands are placed on the accuracy of the mathematical models used in the electromagnetic simulators and the efficiency of their numerical implementation.

Over the past many years, the finite-difference time-domain method (FDTD) has become the prevalent method for solving electromagnetic scattering problems. Not only is it generally applicable to arbitrary geometries, but also it is the most efficient algorithm available, by yielding useful field information at N space points and m time points in a total of only $O(mN)$ operations. Thus, for example, a single time-domain simulation of the response of an electromagnetic system to a finite-duration incident pulse can yield the steady-state results for a large number of different frequencies by Fourier transformation.

The main disadvantage of FDTD is its inefficiency in modeling curved surfaces accurately, since the regular finite-difference mesh used in FDTD requires that curved surfaces be approximated by staircase models. To achieve accurate results using the staircase model, one usually has to use a very fine mesh and, therefore, also a very small time step due to the stability criterion.

Recently, a hybrid-FDTD method appeared in the literature[1] which combines the flexibility of the finite-element method (FEM) in modeling curved surfaces accurately with the computational efficiency of FDTD. It appears that this hybrid-FDTD method, when used in conjunction with high-performance absorbing boundary conditions, is the ideal tool for solving three-dimensional electromagnetic scattering problems arising in lithography simulation accurately and efficiently.

However, the hybrid-FDTD method in its original form is not suitable for DUV lithography simulation. This is because the original formulation cannot handle lossy materials, especially those with negative dielectric constants, such as chromium and silicon, which are commonplace in DUV lithography. The goal of this paper is to extend the orignal hybrid-FDTD formulation to handle lossy materials.

After reviewing the original hybrid-FDTD formulation in Section 2.1, we discuss its extensions to lossy materials with positive and negative dielectric constants separately in Sections 2.2 and 2.3. The issues of mesh generation are discussed briefly in Section 3.1. This is followed in Section 3.2 by a presentation of numerical results comparing the hybrid-FDTD method and standard FDTD for various dielectric materials.

2. THE HYBRID-FDTD METHOD

2.1. The Original Method

The hybrid-FDTD method was originally developed by Wu and Itoh[1] for lossless dielectric objects. Consider a dielectric object bounded by a curved surface S as shown in Fig. 1 The computational domain is divided into two overlapping regions: (i) A regular finite-difference region Ω_1 spanning the interior and exterior of the object at some distance from the surface S, and (ii) an irregular finite-element region Ω_2 spanning the immediate vicinity of S on both of its sides. The two regions overlap in a single layer of finite-difference cells bounded by staircase surfaces Γ_1 and Γ_2 on each side of S.

Suppose the electric field $\mathbf{E}^n$ is known everywhere at time step n. Using the standard Yee algorithm,[2] the magnetic field $\mathbf{H}^{n+\frac{1}{2}}$ at time step $n+\frac{1}{2}$ in the regular region Ω_1, including the overlap region, can be updated. This in turn allows the electric field $\mathbf{E}^{n+1}$ in Ω_1, including the boundary Γ_1, to be updated. The electric field $\mathbf{E}^{n+1}$ in the irregular region Ω_2 is then updated by solving the weighted-residual problem

$$\frac{\partial^2}{\partial t^2}\int_\Omega \epsilon \mathbf{E}^a \cdot \mathbf{E}\, d\Omega \;=\; -\int_\Omega \frac{1}{\mu}\nabla\times\mathbf{E}^a\cdot\nabla\times\mathbf{E}\, d\Omega\ , \tag{1}$$

using the electric field $\mathbf{E}^{n+1}$ on Γ_1 as boundary condition and the previous electric fields $\mathbf{E}^n$ and $\mathbf{E}^{n-1}$ in Ω_2 as initial condition. Once the electric field at time step $n+1$ becomes available everywhere, the time-marching can be continued for the next time step.

To solve the weighted-residual problem Eq. (1), the irregular region Ω_2 is subdivided into many small tetrahedral elements and the electric field in the elements is expanded in Whitney vector basis functions $\mathbf{W}_j$,[3] with the electric field components E_j along the element edges j as the expansion coefficients. Next, the time derivative in Eq. (1) is approximated by the central difference operator and the Newmark-Beta method[1] is applied to obtain an unconditionally stable, second-order accurate, implicit time-marching scheme,

$$\left([C]+\frac{\Delta t^2}{4}[D]\right)\bar{E}^{n+1} \;=\; 2\left([C]-\frac{\Delta t^2}{4}[D]\right)\bar{E}^{n}-\left([C]+\frac{\Delta t^2}{4}[D]\right)\bar{E}^{n-1}\ . \tag{2}$$

Here the matrices $[C]$ and $[D]$ are given by

$$[C]_{ij} \;=\; \int_\Omega \epsilon_0\epsilon_r \mathbf{W}_i\cdot\mathbf{W}_j\, d\Omega\ , \tag{3}$$

$$[D]_{ij} \;=\; \int_\Omega \frac{1}{\mu}\nabla\times\mathbf{W}_i\cdot\nabla\times\mathbf{W}_j\, d\Omega\ , \tag{4}$$

where ϵ_r is the dielectric constant and $\bar{E}^n$ is the vector of expansion coefficients at time step n.

The above formulation of Wu and Itoh is applicable only to lossless dielectric objects with positive dielectric constants ϵ_r. The objects encountered in lithography simulation, however, are often lossy and, furthermore, may have negative dielectric constants, especially at DUV wavelengths. We next discuss the extensions of the formulation of Wu and Itoh to lossy media with positive and negative dielectric constants separately.

2.2. Extension to Lossy Medium with Positive Dielectric Constant

A material with positive dielectric constant is one for which the real part n of its complex refractive index is greater than the imaginary part κ. Such is the case for weakly absorbing materials such as photoresist and silicon nitride. This kind of material can be modeled in the time domain by adding a conductivity term to the electric-field updating equation. The dielectric constant ϵ_r and conductivity σ are related to the complex refractive index $n+j\kappa$ by

$$\epsilon_r \;=\; n^2-\kappa^2\ , \tag{5}$$

$$\sigma \;=\; 2n\kappa\,\omega_0\epsilon_0\epsilon_r\ , \tag{6}$$

where ω_0 is the frequency of interest.

By using exponential time stepping,[4] the updating equation for the electric field in the irregular region becomes

$$\left([C_+]+\frac{\Delta t^2}{4}[D]\right)\bar{E}^{n+1} \;=\; 2\left([C_0]-\frac{\Delta t^2}{4}[D]\right)\bar{E}^{n}-\left([C_-]+\frac{\Delta t^2}{4}[D]\right)\bar{E}^{n-1}\ , \tag{7}$$

where the matrices $[C_\pm]$ and $[C_0]$ are given by

$$[C_\pm]_{ij} = \int_\Omega \epsilon_0\epsilon_r \exp\left(\pm\frac{\sigma\Delta t}{2\epsilon_0\epsilon_r}\right) \mathbf{W}_i \cdot \mathbf{W}_j \, d\Omega \ , \tag{8}$$

$$[C_0]_{ij} = \int_\Omega \epsilon_0\epsilon_r \cosh\left(\frac{\sigma\Delta t}{2\epsilon_0\epsilon_r}\right) \mathbf{W}_i \cdot \mathbf{W}_j \, d\Omega \ . \tag{9}$$

The time-marching scheme Eq. (7) is unconditionally stable as long as $\epsilon_r > 0$.

2.3. Extension to Lossy Medium with Negative Dielectric Constant

A material for which $n < \kappa$ has a negative dielectric constant according to Eq. (5). Silicon, chromium and tungsten are examples of such materials at DUV wavelengths. This type of material can be modeled in the time domain by an unmagnetized plasma,[5] with a complex dielectric function

$$\epsilon_r(\omega) = 1 - \frac{\omega_p^2}{\omega(\omega + j\nu_c)} \ . \tag{10}$$

The plasma frequency ω_p and collision frequency ν_c appearing in Eq. (10) are related to the complex refractive index of the material at the frequency ω_0 of interest by

$$\frac{\omega_p^2}{\omega_0^2} = 1 + \kappa^2 - n^2 + \frac{4n^2\kappa^2}{1 + \kappa^2 - n^2} \ , \tag{11}$$

$$\frac{\nu_c}{\omega_0} = \frac{2n\kappa}{1 + \kappa^2 - n^2} \ . \tag{12}$$

The weighted-residual problem to be solved in the irregular plasma region is

$$\begin{aligned}\frac{\partial^2}{\partial t^2}\int_\Omega \epsilon_0 \mathbf{E}^a \cdot \mathbf{E} \, d\Omega &= -\int_\Omega \frac{1}{\mu}\nabla\times\mathbf{E}^a \cdot \nabla\times\mathbf{E} \, d\Omega - \int_\Omega \omega_p^2 e^{-\nu_c t}\mathbf{E}^a\cdot\mathbf{E}\, d\Omega \\ &\quad + \int_{-\infty}^{t} dt' \int_\Omega \nu_c\omega_p^2 e^{-\nu_c t'}\mathbf{E}^a\cdot\mathbf{E}(t-t')\, d\Omega \ ,\end{aligned} \tag{13}$$

in which a convolution term appears due to the frequency dependence of the plasma dielectric function Eq. (10). Expanding the electric field $\mathbf{E}$ in Whitney basis functions and applying the Newmark-Beta method, we obtain the following second-order accurate, implicit time-marching scheme:

$$\begin{aligned}\left([C] + \frac{\Delta t^2}{4}\left\{[D] + \left[\chi^{(1)}\right]\right\}\right)\bar{E}^{n+1} &= 2\left([C] - \frac{\Delta t^2}{4}\left\{[D] + \left[\chi^{(1)}\right]\right\}\right)\bar{E}^n \\ &\quad - \left([C] + \frac{\Delta t^2}{4}\left\{[D] + \left[\chi^{(1)}\right]\right\}\right)\bar{E}^{n-1} + \bar{\Psi}^n \ .\end{aligned} \tag{14}$$

where $[C]$ is given by Eq. (3) with $\epsilon_r = 1$ and the matrix $\left[\chi^{(1)}\right]$ is given by

$$\left[\chi^{(1)}\right]_{ij} = \int_\Omega \left(\frac{1 - e^{-\nu_c\Delta t}}{\nu_c\Delta t}\right) \mathbf{W}_i \cdot \mathbf{W}_j \, d\Omega \ , \tag{15}$$

The vector $\bar{\Psi}^n$ appearing in Eq. (14) is define as

$$\bar{\Psi}^n = \sum_{m=1}^{n-1} \left[\chi_m^{(2)}\right] \bar{E}^{n-m} \ , \tag{16}$$

where the matrix $\left[\chi_m^{(2)}\right]$ is given by

$$\left[\chi_m^{(2)}\right]_{ij} = \int_\Omega 2\left[\frac{\cosh(\nu_c\Delta t) - 1}{\nu_c\Delta t}\right]\omega_p^2\Delta t^2 e^{-\nu_c m\Delta t} \, \mathbf{W}_i \cdot \mathbf{W}_j \, d\Omega \ . \tag{17}$$

Using the technique of Luebbers et al.,[5] the vector $\bar{\Psi}^n$ can be computed recursively by

$$\bar{\Psi}^n = \left[\chi_1^{(2)}\right] \bar{E}^{n-1} + e^{-\nu_c \Delta t} \bar{\Psi}^{n-1} \quad . \tag{18}$$

The same plasma model Eq. (10) can be applied to the regular FDTD region in the interior of the object. However, the traditional FDTD implementation of this model[5] is only first-order accurate in time, due in part to the use of the rectangular rule for the convolution integral. Instead, by assuming the electric field to vary linearly with time between successive time steps and performing the resulting convolution integral exactly, the following second-order accurate updating equation for the electric field in the interior FDTD region is obtained:

$$\mathbf{E}^{n+1} = \frac{1}{1+\frac{1}{2}\omega_p^2 \Delta t^2 \alpha_0} \left\{ \left[1 - \frac{1}{2}\omega_p^2 \Delta t^2 \left(\alpha_0 + \alpha_1 e^{-\nu_c \Delta t}\right) \right] \mathbf{E}^n - \frac{1}{2}\omega_p^2 \Delta t^2 \mathbf{\Phi}^n + \frac{\Delta t}{\epsilon_0} \operatorname{curl} \mathbf{H}^{n+\frac{1}{2}} \right\} \quad , \tag{19}$$

where

$$\alpha_0 = \frac{1}{\nu_c \Delta t} \left[1 - \left(\frac{1 - e^{-\nu_c \Delta t}}{\nu_c \Delta t} \right) \right] \quad , \tag{20}$$

$$\alpha_1 = 2 \left[\frac{\cosh(\nu_c \Delta t) - 1}{(\nu_c \Delta t)^2} \right] \quad . \tag{21}$$

The vector $\mathbf{\Phi}^n$ appearing in Eq. (19) is defined as

$$\mathbf{\Phi}^n = \sum_{m=1}^{n-1} \alpha_1 \left(1 + e^{-\nu_c \Delta t}\right) e^{-\nu_c m \Delta t} \, \mathbf{E}^{n-m} \quad , \tag{22}$$

and can be computed recursively by

$$\mathbf{\Phi}^n = e^{-\nu_c \Delta t} \left[\alpha_1 \left(1 + e^{-\nu_c \Delta t}\right) \mathbf{E}^{n-1} + \mathbf{\Phi}^{n-1} \right] \quad . \tag{23}$$

To our knowledge, the second-order accurate updating equation Eq. (19) has not appeared before in the literature.

3. RESULTS

We tested the formulations discussed in Sections 2.1 to 2.3 with the problem of electromagnetic scattering by a dielectric sphere, for which the exact solution is known. The diameter of the sphere was 0.06 μm and the wavelength was 0.248 μm.

3.1. Mesh Generation

The first step in the computation was to generate a high-quality mesh for the three-dimensional irregular region Ω_2 shown in Fig. 1. After subdividing the surface of the sphere into a large number of small triangles, an unstructured tetrahedral mesh was generated in Ω_2 conforming to the surface triangulation of the sphere and the staircase boundaries Γ_1 and Γ_2, using our automatic mesh-generation software.

The quality Q of our mesh was measured by the *minimum* of the sines of all the dihedral angles in the mesh, where $0 \leq Q \leq 1.0$. This quality measure was chosen to bias against elements with too large ($\theta_{\min} \approx 180^o$) or too small ($\theta_{\min} \approx 0^o$) dihedral angles, which would lead to poor accuracy of the finite-element interpolation or poor conditioning of the finite-element matrix, respectively.[6] It was found that our as-generated mesh had a quality Q of only 0.073, indicating the presence of poorly shaped elements in the mesh.

To remove the poorly shaped elements, we performed mesh improvement on the as-generated mesh in two steps. In the first step, the sub-mesh belonging to each *edge* in the mesh, consisting of all the tetrahedra adjacent to that edge, was examined. The edge was deleted and replaced by one or more new edges if, by doing so, the quality of the sub-mesh was improved. In the second step, the cluster belonging to each *node*, consisting of all the tetrahedra adjacent to that node and its nearest neighbors, was examined. If the quality of the cluster was below a certain threshold, the nodes in the cluster were moved to new positions which maximized the quality of the cluster. It was found that after a single pass through our mesh-improvement routine, the quality of the mesh increased to $Q =$

0.335, which was deemed satisfactory for our computation. The final mesh is shown in Fig. 2 and consists of 1195 nodes, 7158 edges and 5485 tetrahedra.

The above finite-element mesh was embedded in a regular finite-difference mesh with $20 \times 20 \times 20$ cells. For simplicity, the first-order Higdon absorbing boundary condition[8] was used on all six sides of the computational domain, which measured 0.2μm $\times 0.2\mu$m $\times 0.2\mu$m. A Huygens surface[9] located two cells interior to the outermost boundaries was used to excite the domain with various Gaussian pulses.

3.2. Numerical Results

3.2.1. Lossless Dielectric

We first compared our results with those of Wu and Itoh, who used a lossless dielectric sphere of refractive index $n_1 = 3.0$ and a Gaussian pulse with finite d.c. content,

$$\mathbf{E}^n_{\text{inc}} = \hat{\mathbf{x}}\, e^{-\left[3\left(\frac{n}{n_0}-1\right)\right]^2}, \tag{24}$$

where $n_0 = 33$. The computed results are shown in Fig. 3. Fig. 3a shows the total time-domain waveform at the center of the sphere, while Fig. 3b shows the scattered waveform at a point 0.09μm in front of the sphere. Also shown in the figures are the exact Mie solution[7] and the results obtained with standard FDTD using the same mesh spacing as hybrid-FDTD in the regular region Ω_1, namely, $20 \times 20 \times 20$ cells, or roughly 1/8 of the wavelength λ_1 inside the dielectric. The results of Figs. 3a and 3b are in good agreement with those of Wu and Itoh.[1] This verifies the correctness of our computer program.

Next, the frequency-domain scattering cross section was obtained by Fourier transformation of the corresponding time-domain result. The hybrid-FDTD result is shown in Fig. 3c, together with the exact Mie solution and the results obtained with standard FDTD using $20 \times 20 \times 20$ and $40 \times 40 \times 40$ cells, respectively. It can be seen that, compared with the exact result, the hybrid-FDTD method with a coarse mesh spacing of $\lambda_1/8$ gave much better accuracy than FDTD with the same mesh spacing, and roughly the same accuracy as FDTD with the finer mesh spacing of $\lambda_1/16$. The small discrepancy between the hybrid-FDTD result and the exact result is due in part to the approximate absorbing boundary conditions used.

3.2.2. Lossy Dielectric with Positive Dielectric Constant

We tested the formulation of Section 2.2 by using a lossy dielectric sphere of refractive index $n_1 = 2.0 + j0.5$. The time derivative of a Gaussian pulse was used for excitation to avoid introducing a d.c. offset into the solution,

$$\mathbf{E}^n_{\text{inc}} = -\hat{\mathbf{x}}\, 3\sqrt{2e}\left(\frac{n}{n_0}-1\right) e^{-\left[3\left(\frac{n}{n_0}-1\right)\right]^2}, \tag{25}$$

where $n_0 = 33$. The computed time-domain waveforms are shown in Figs. 4a and 4b, together with the exact results and the results obtained with standard FDTD using the same mesh spacing as hybrid-FDTD, or roughly 1/12 of the wavelength inside the dielectric. It can be seen that the hybrid-FDTD and FDTD results are both in good agreement with the exact results, although the FDTD results have slightly more overshooting at the valleys of the waveforms.

The result for the Fourier transformed scattering cross section is shown in Fig. 4c, together with the FDTD results obtained with a coarse and a fine mesh spacing. It can be seen that, as in the lossless dielectric case, the hybrid-FDTD method with a coarse mesh spacing of $\lambda_1/12$ gave much better accuracy than FDTD with the same mesh spacing, and roughly the same accuracy as FDTD with the finer mesh spacing of $\lambda_1/24$.

3.2.3. Lossy Dielectric with Negative Dielectric Constant

We tested the formulation of Section 2.3 by using a lossy dielectric sphere of refractive index $n_1 = 0.85 + j2.01$, which is the refactive index of chromium at 0.248 μm.[10] The time-derivative Gaussian pulse Eq. (25) with zero d.c. content was used for excitation to avoid the singularity of the plasma dielectric function Eq. (10) at $\omega = 0$.

The computed time-domain waveforms are shown in Figs. 5a and 5b, together with the exact results and the results obtained with standard FDTD using the same mesh spacing as hybrid-FDTD, or roughly 1/29 of the wavelength inside the dielectric sphere. It can be seen that, whereas the hybrid-FDTD results are in good agreement with the exact results for all times, the FDTD results show marked departures from the exact results at late times.

The result for the Fourier transformed scattering cross section is shown in Fig. 5c, together with the FDTD results obtained with a coarse, a fine and a *very* fine mesh spacing. It can be seen that, whereas the hybrid-FDTD result is in good agreement with the exact result, the FDTD results for all three mesh spacings, namely, $\lambda_1/29, \lambda_1/58$ and $\lambda_1/116$, show large departures from the exact result. Since the second-order accurate updating equation Eq. (19) was used for the FDTD computations, these departures cannot be due to inaccurate implementation of the plasma dispersion model of Section 2.3, but, rather, must be due to inaccuracy of the staircase model of the spherical surface used in standard FDTD. These results highlight the need to use the hybrid-FDTD method to model curved surfaces accurately in the case of lossy dielectric materials with negative dielectric constants.

4. CONCLUSIONS

Extensions of the original hybrid-FDTD method to handle lossy materials with positive and negative dielectric constants have been discussed separately. The correctness of our computer program has been verified by comparing our computed results with those in the literature and with the exact results. Our results have shown that, for lossless dielectric and lossy material with positive dielectric constant, the hybrid-FDTD method is much more accurate than standard FDTD when the same mesh spacing is used in both methods, while the two methods have roughly the same accuracy when the mesh spacing used in standard FDTD is half that used in hybrid-FDTD. For lossy material with negative dielectric constant, the difference between the two methods is much more pronounced. In this case, the hybrid-FDTD method with a mesh spacing of Δ is much more accurate than standard FDTD even when a mesh spacing of $\frac{1}{4}\Delta$ is used in the latter method. These results indicate that the hybrid-FDTD method is far superior to standard FDTD for lithography simulation at DUV wavelengths, where lossy materials with negative dielectric constants are commonplace.

5. ACKNOWLEDGEMENT

This research was supported by AFOSR/DARPA MURI grant no. 98-1-0525.

REFERENCES

1. R. B. Wu and T. Itoh, "Hybrid finite-difference time-domain modeling of curved surfaces using tetrahedral edge elements", *IEEE Trans. Antennas Propagat.*, Vol. 45, pp. 1302-1309 (1997).
2. K. S. Yee, "Numerical solution of initial boundary value problems in isotropic media" *IEEE Trans. Antennas Propagat.*, Vol. 14, pp. 302-307 (1966).
3. A. Bossavit, "Simplicial finite elements for scattering problems in electromagnetism", *Comput. Methods Appl. Mech. Engrg.*, Vol. 64, pp. 299-316 (1989).
4. R. Holland, "Finite-difference time-domain (FDTD) analysis of magnetic diffusion", *IEEE Trans. Electromagnetic Compatibility*, Vol. 36, pp. 32-39 (1994).
5. R. J. Luebbers, F. Hunsberger and K. S. Kunz, "A frequency-dependent finite-difference time-domain formulation for transient propagation in plasma", *IEEE Trans. Antennas Propagat.*, Vol. 39, pp. 29-34 (1991).
6. I. Fried, "Condition of finite element matrices generated from nonuniform meshes", *AIAA Journal*, Vol. 10, pp. 219-221 (1972).
7. J. A. Stratton, "Electromagnetic Theory" (McGraw-Hill, 1941).
8. R. L. Higdon, "Absorbing boundary conditions for difference approximations to the multi-dimensional wave equation", *Math. Comp.*, Vol. 47, pp. 437-459 (1986).
9. R. Holland and J. W. Williams, "Total-field versus scattered-field finite-difference codes: A comparative assessment", *IEEE Trans. Nuclear Science*, Vol. 30, pp. 4583-4588 (1983).
10. A. K. Wong and A. R. Neureuther, "Rigorous three-dimensional time-domain finite-difference electromagnetic simulation for photolithographic applications", *IEEE Trans. Semiconductor Manufacturing*, Vol. 8, pp. 419-431 (1995).

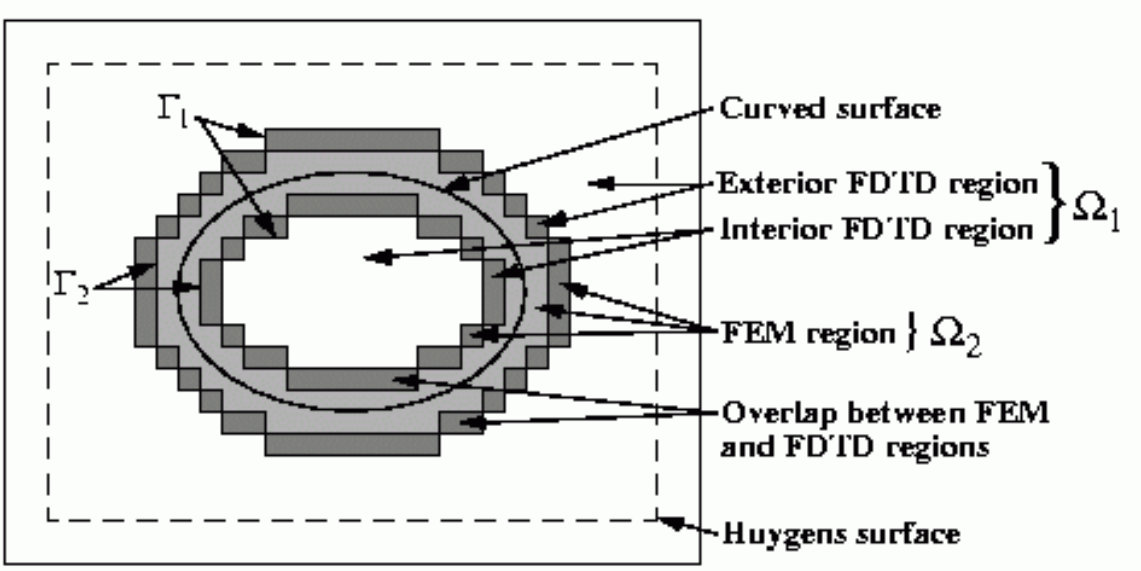

Figure 1. The hybrid-FDTD computational domain consisting of overlapping FDTD(Ω_1) and FEM(Ω_2) regions. Γ_1 and Γ_2 are the exterior and secondary boundaries, respectively, of the overlap region. An incident wave is applied to the Huygens surface.

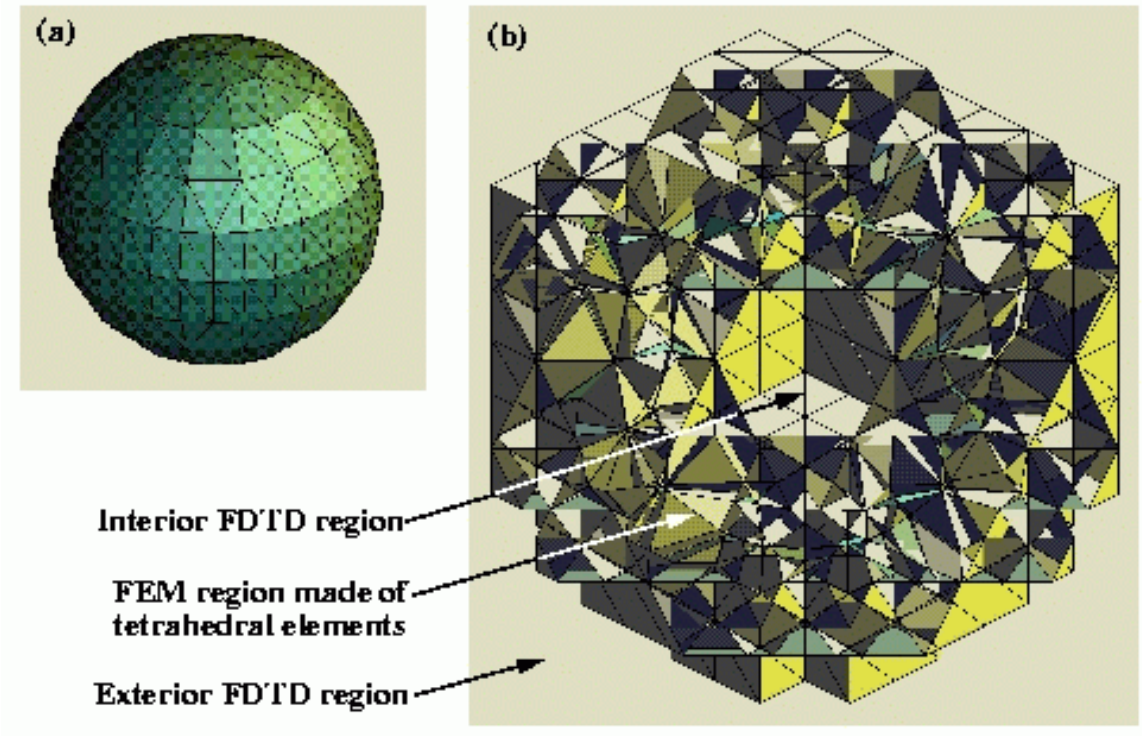

Figure 2. (a):The surface of a sphere of diameter 0.06 μm modeled by 352 triangles. (b):Cutaway view of the FEM mesh used in the hybrid-FDTD method.

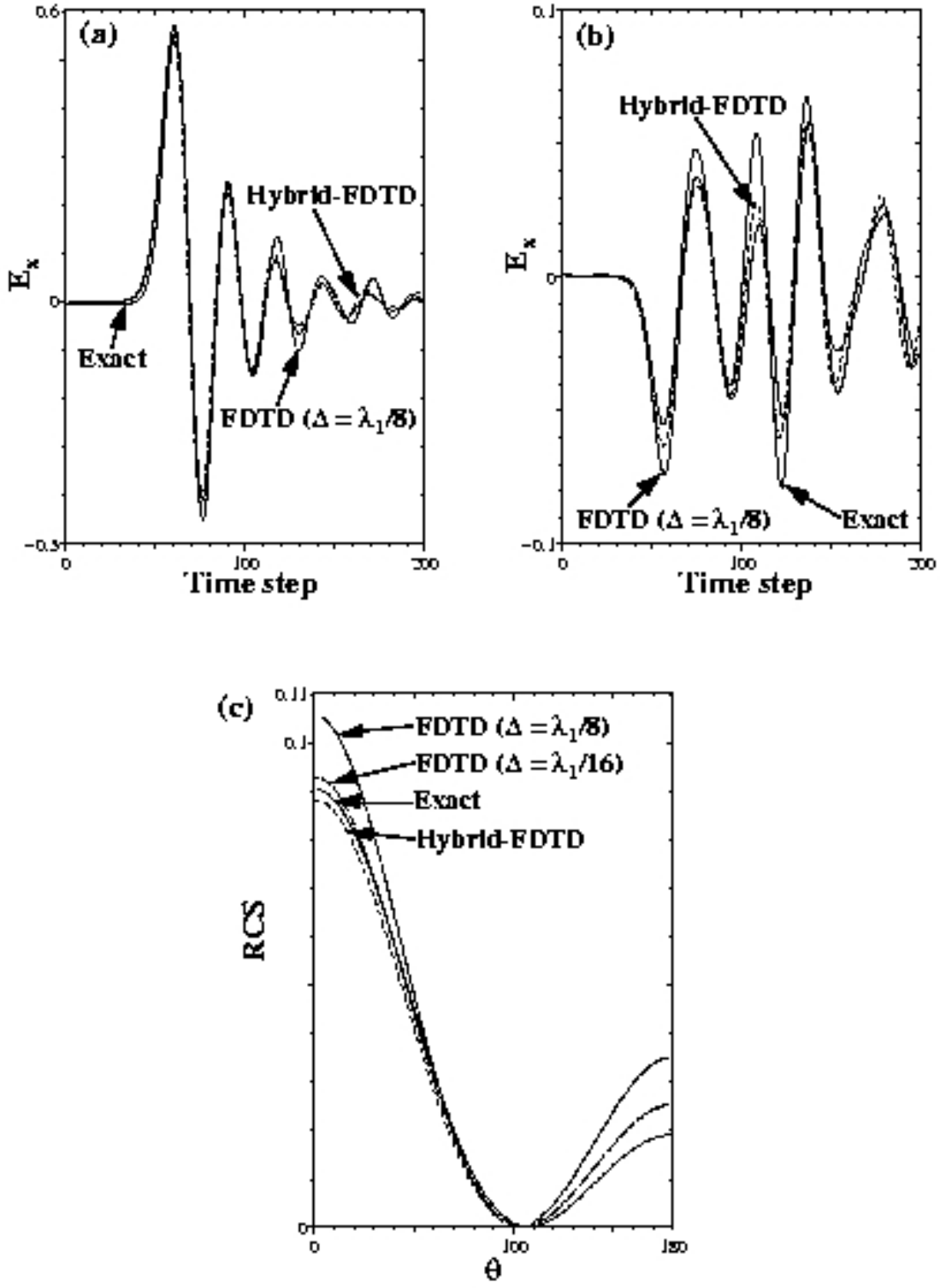

Figure 3. Results for a lossless dielectric sphere of refractive index $n_1 = 3.0$. (a) and (b): Time-domain waveforms at center of sphere and at a point 0.09 μm in front of the sphere. (c):Radar cross section obtained by Fourier transformation of the time-domain results.

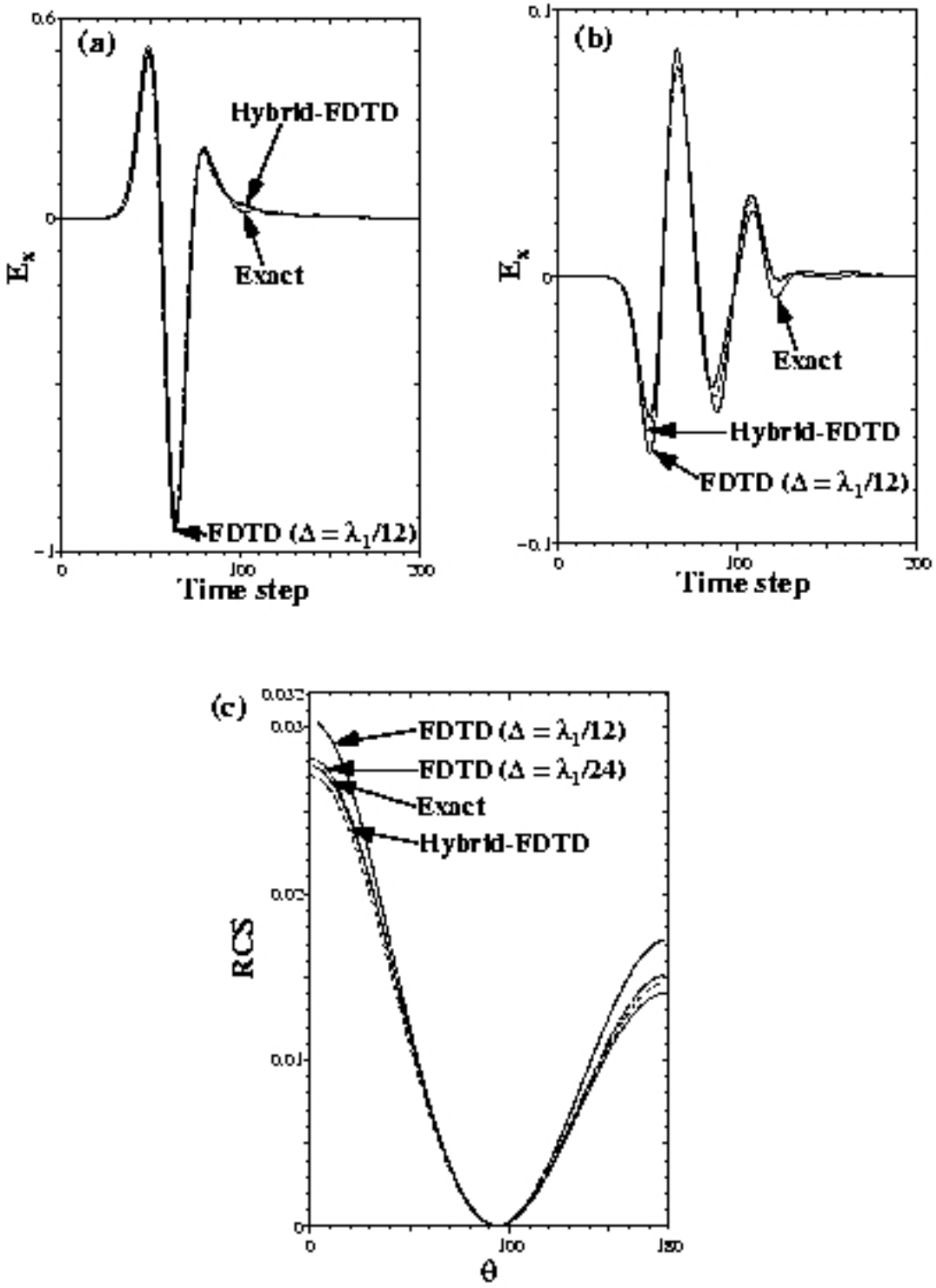

Figure 4. Results for a lossy dielectric sphere of refractive index $n_1 = 2.0 + j0.5$. (a) and (b): Time-domain waveforms at center of sphere and at a point 0.09 μm in front of the sphere. (c):Radar cross section obtained by Fourier transformation of the time-domain results.

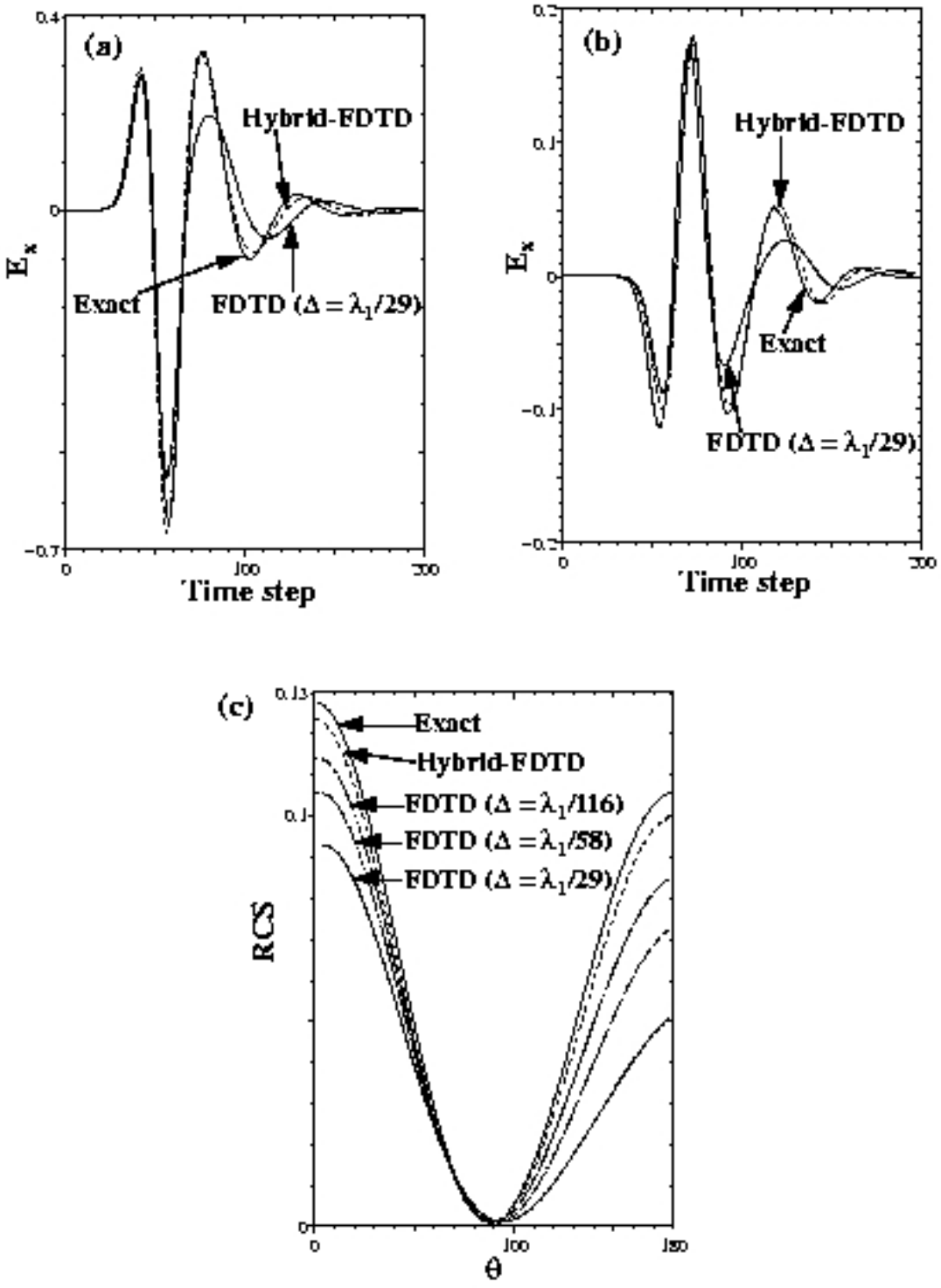

Figure 5. Results for a lossy dielectric sphere of refractive index $n_1 = 0.85 + j2.01$. (a) and (b): Time-domain waveforms at center of sphere and at a point 0.09 μm in front of the sphere. (c):Radar cross section obtained by Fourier transformation of the time-domain results.